Joint segmentation and characterization of the dermis in 50 MHz ultrasound 2D and 3D images of the skin

Bruno Sciolla, Jimmy Le Digabel, Gwendal Josse, Thibaut Dambry, Benoit Guibert, Philippe Delachartre

Available online at www.sciencedirect.com
ScienceDirect
Computers in Biology and Medicine 00 (2018) 1–17
Comput Biol Med

Joint segmentation and characterization of the dermis in 50 MHz ultrasound 2D and 3D images of the skin

Bruno Sciolla[a], Jimmy Le Digabel[b], Gwendal Josse[b], Thibaut Dambry[c], Benoît Guibert[c], Philippe Delachartre[a,*]

[a] *CREATIS laboratory, INSA Lyon, France*
[b] *Centre de Recherche sur la Peau, Pierre Fabre Dermo-Cosmétique, Toulouse, France*
[c] *Atys Medical, Soucieu-en-Jarrest, France*

Abstract

We propose a novel joint segmentation and characterization algorithm for the assessment of skin aging using 50 MHz high-frequency ultrasound images. The proposed segmentation method allows a fine determination of the envelope signal's statistics in the dermis as a function of depth. The sequence of statistical estimates obtained is then combined into a single aging score. The segmentation is based on tailored recursive non-linear filters inspired from deep learning methods. The epidermis and the dermis are jointly segmented with a non-parametric active contour combining a texture criterion, an epidermis indicator map and the geometric constraint of horizontal continuity. The algorithm is designed to apply to 2D and 3D images as well. We evaluated skin photo-aging on ultrasound images with an experimental study on a cohort of 76 women separated into 2 groups of different ages. Two aging scores are computed from the images: local dermal contrast and skin roughness. We show that these scores are much better at identifying the two groups (p-value $\approx 10^{-6}$) than the previously used MGVR indicator (p-value 0.046). Moreover, we find that a combined score more reliably evaluates skin photo-aging, with 84% success, than a scoring of the ultrasound images by 4 experts.

Keywords: Ultrasound, Characterization, Dermatology, Segmentation, Level-set, Skin aging, Nakagami distribution, High-frequency ultrasound, Nonlinear filter, Recursive filter

1. Introduction

The study of skin aging is a central and active topic of dermatology and cosmetics ([1, 2]). Aged skin is susceptible to a variety of disorders of diverse severity, such as pervasive dryness and itching, infections, autoimmune disorders and vascular complications ([3]). In the United States, most people over 65 suffer from at least one skin disorder ([3]). In particular, photo-aging of the skin due to exposure to ultraviolet (UV) radiation is a cause of malignant tumors of the skin: 85% of melanomas are attributed to excess solar irradiation ([4]). Non-melanoma skin cancers are also very common and related to photo-aging. On average one in five individuals will develop one in their lifetime ([5]), and developping computer-assisted tools for the diagnosis and treatment of skin cancers is an active research topic ([6]).

Several modalities are used to characterize skin aging. Histology is one of the reference methods, but it is only performed for medical diagnoses and it causes scarring. There is thus a need for non-invasive methods that can evaluate excessive photo-aging in order to alert us before the development of serious skin disorders. Different non-invasive techniques have been used in previous studies to quantify skin aging: blood flow, pH, dermal thickness,

*Corresponding author
Email address: philippe.delachartre@creatis.insa-lyon.fr (Philippe Delachartre)

protein, glycosaminoglycan, water, and lipid content and structure. Other techniques, such as ultrasound echogenicity ([1, 7]) and reflectance confocal microscopy ([8, 9, 10]), can provide advanced visualisation of the skin to help physicians perform their diagnosis. Reflectance confocal microscopy has a maximum depth investigation of $\sim 300\,\mu$m or less. For example, Longo et al ([10]) used this technique to investigate the superficial layers of the skin, with a maximum depth of $100\,\mu$m. But skin photo-aging mainly affects the dermal fibers located below the epidermis. High-frequency ultrasound allows this analysis of the whole dermis, with a maximum depth of approximately 3 mm at 50 MHz.

In ultrasound images, a low-echoic band on the top of the dermis, called SLEB (subepidermal low-echoic band) has been shown to be caused by chronic UV-exposure and for this reason is associated with skin photo-aging ([11, 12, 13, 14]). The presence of this SLEB has been attributed to an alteration of collagen fibers and an accumulation of free water in the papillary dermis ([12]). The non-organized collagen and high water content cause a reduction of reflected ultrasound waves. Moreover, the elastic fibers play a crucial role in the elasticity of the skin ([15]). The alteration of these fibers enhances skin wrinkling, as the dermis loses its elastic properties.

In previous studies, the accuracy of the SLEB evaluation was limited by the image resolution. Most studies used 20 MHz or lower frequency ultrasound ([11]), whereas in this study we use a 50 MHz ultrasound system, which offers the best compromise between depth and resolution for the study of the dermis.

In this article, we study photo-aging using an automatic joint segmentation and characterization method. This method has been applied to a cohort of 76 healthy volunteers divided into two age classes. To limit the data variability, all volunteers were non-smoking women of phototype II and III ([16]) with no dermatosis. All acquisitions have been performed on the exterior forearm, which is a naturally photo-exposed area.

Because the contrast in the SLEB area is very low, standard sliding-window techniques used in previous studies ([17]) can fail to capture the effects of aging. Instead, we propose a two-step procedure: first, segmentation of the dermis and second, the characterization analysis. Yet the automatic segmentation of the dermis and the epidermis is also a challenging task because of the artifacts found in 50 MHz clinical images - membrane artifacts, bubbles, slanted skin surface.

The proposed method for characterizing the skin brings several major improvements:

1. The signal statistics of the dermis are studied accurately layer by layer. This is made possible by the development of an automatic, accurate segmentation method. As we shall see, the statistics of the signal vary strongly with depth. The use of an automatic segmentation to define the region of interest is crucial to extract significant scores - we refer to this as a *joint segmentation and characterization*. Most previous characterization studies use a sliding window, which has been shown to induce errors of interpretation for inhomogeneous tissues ([17]). Recent works have tried to alleviate this issue by using coarse-to-fine sliding windows ([18]). Using joint segmentation and characterization, our method goes one step further and estimates the exact location of the different tissues prior to characterization. The work of Byra et al ([19]) proposes a similar idea, but the segmentation is performed with k-means, a much more simple method.
2. The segmentation is highly resistant to artifacts thanks to the use of elaborate non-linear filters and a multiple loss level-set segmentation algorithm.
3. The proposed method is designed for 2D as well as 3D images. 3D images provide more accurate statistics, as a single 3D image contains 300 2D images. Moreover, the proposed score is based on fits to a Nakagami law, known to be a robust estimator of the envelope statistics ([20, 17]).

The article is structured as follows. The ultrasound data is introduced first. Then the segmentation method is described in detail, in particular the non-linear filters and the active contour segmentation of the epidermis-dermis frontier. The characterization, which is applied to thin dermal layers, is then explained. The envelope is studied with a fit to a Nakagami distribution and all parameters are combined into an aging score.

The proposed aging scores and the segmentation step are validated on the clinical dataset of 76 volunteers presented in the section Results. The accuracy of the segmentation is evaluated using contours drawn by 2 experts, and the method is illustrated on two 3D images. The scores are finally validated on the experimental data, compared with the previous score and evaluated by 4 experts with a blind classification.

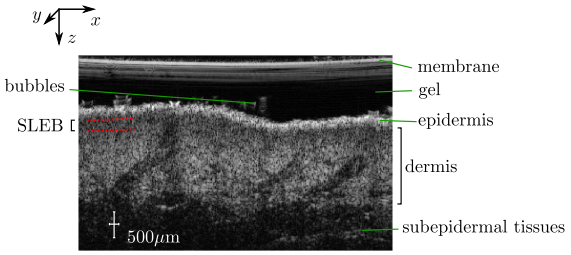

Figure 1. An example of a dermis image at 50MHz, displaying a clear SLEB. There is a membrane echo on top of the image.

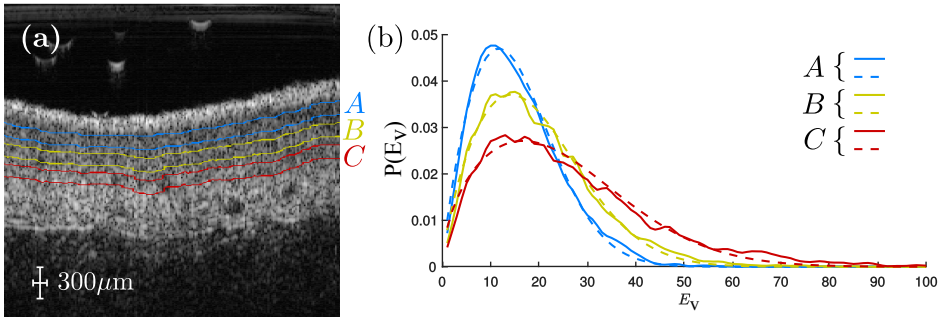

Figure 2. **(a)** Image of the skin with three layers of equal width at increasing depth A, B, C drawn by an expert. **(b)** Histograms of the pixels in the echographic image (or more precisely, of the envelope image $E_v(z, x)$), for each region A, B, C depicted in the image **(a)**. The full line is the raw histogram, the dashed lines are fits to a Nakagami distribution defined later in equation (23).

2. Method

2.1. 50 MHz images of the skin

In this study, the raw radiofrequency signal is available, allowing us to compute the envelope image $E_v(x, y, z)$ and the normalized log-compressed image $I(x, y, z) \in [0, 1]$, where z spans the longitudinal axis, x spans the lateral axis and y the remaining orthogonal lateral axis for 3D images. -A typical example of a 50 MHz image of the skin is shown in Fig. 1, where the epidermis, dermis and the SLEB (sub-epidermal low-echoic band) are indicated. Qualitatively, the aging in the dermis is associated with the SLEB layer at the top of the dermis shown in Fig. 2(a).

Figure 2(b) shows the histogram of the echo envelope $P(E_v)$ in three thin layers, and a fit to the Nakagami distribution. Notice that the Nakagami distribution provides a good fit to the empirical distribution of the envelope. This is possible thanks to the careful definition of very thin parallel layers in the dermis.

In the following, we shall see how these parallel layers can be detected entirely automatically, and how a quantitative score for skin aging can be derived from their statistical characterization.

The following section describes the proposed processing chain for the joint segmentation and characterization of the dermis, depicted in Fig. 3. The first step is to build an epidermis indicator map using non-linear filters. Then, a joint segmentation of the epidermis and dermis is performed. Finally, the thin layers of the dermis are analyzed using fits to a Nakagami distribution, and an aging score is derived.

2.2. Epidermis indicator map

In ultrasound 50 MHz images of the skin, the epidermis is a hyperechoic, continuous region at the top of the image. It can not be trivially identified because of the occasional presence of bubbles, membrane echoes and the possible slanting of the dermis with respect to the probe, as illustrated in Fig. 4(a). To tackle this, a recursive approach with non-inear filters is proposed for the automatic detection of the epidermis.

The normalized log-compressed image $I(x, y, z) \in [0, 1]$ is transformed via a series of non-linear filters in order to design an indicator map of the epidermis $M^{\text{epi}}(x, y, z)$. The first map is designed to identify the vertical gradient M^{ver} signaling the epidermis. The second is a map to identify membrane echo artifacts M^{mem}. The M^{ver} and M^{mem} maps are

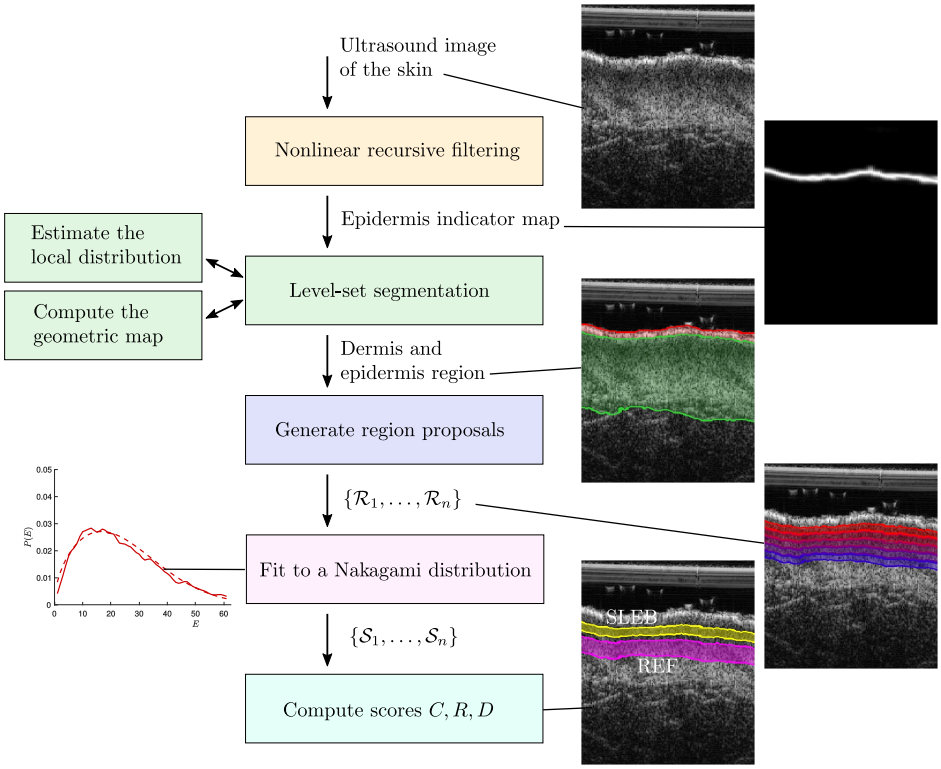

Figure 3. Overview of the processing chain. The non-linear filter are presented in section 2.2, the segmentation in section 2.3. The definition of the regions of interest and the fit to a Nakagami distribution are in section 2.4. The parameters are combined into different scores of aging: contrast C, roughness R and a combined criterion D.

combined to define an epidermis map M^{com}. This is then refined to eliminate isolated artifacts, obtaining the clean epidermis map M^{epi}:

$$M^{\text{ver}} = \text{Norm}\left(|\overline{V} \star I| \times I\right) \tag{1}$$

$$M^{\text{mem}} = \text{Norm}\left(|I - \overline{H} \star I|\right) \tag{2}$$

$$M^{\text{com}} = \text{Norm}\left(\overline{G}(|M^{\text{mem}}|^{1/2} \times M^{\text{ver}})\right) \tag{3}$$

$$M^{\text{epi}} = \mathcal{N}^{(5)}(M^{\text{com}}) \tag{4}$$

In the above, Norm is a longitudinal normalization:

$$\text{Norm}(Y(x, y, z)) = \frac{Y(x, y, z)}{\max_z Y(x, y, z)} \tag{5}$$

The operator $\star$ is a 2D convolution with discrete filters in the (z, x) plane and $\times$ is the pixel by pixel product:

- $\overline{G}$ is a Gaussian filter of size 6×6 of width $\sigma = 1.2$ (real size of 180×600 μm).
- $\overline{V}$ is a 24×1 (shifted) vertical derivative filter (700 μm).
- $\overline{H}$ is a 1×20 horizontal averaging filter (2 mm).
- $\overline{B}$ is an indicator 10×10 filter, positive if the neighbors at a distance of 5 pixels (500 μm) to the left or to the right of a given point are positive.

The filters are defined as:

$$\overline{V} = \frac{1}{16}\begin{bmatrix} 1 \\ \dots \\ 1 \\ -1 \\ \dots \\ -1 \\ 0 \\ \dots \\ 0 \end{bmatrix}; \quad \overline{H} = \frac{1}{20}\begin{bmatrix} 1 & \dots & 1 \end{bmatrix}; \quad \overline{B} = \frac{1}{20}\begin{bmatrix} 1 & 0 & \dots & 0 & 1 \\ | & | & & | & | \\ 1 & 0 & \dots & 0 & 1 \end{bmatrix} \tag{6}$$

The neighbor detection map $\mathcal{N}^{(n)}$ is defined recursively as:

$$\mathcal{N}^{(1)}(X) = \text{Norm}\left(\left|\overline{B} \star X\right| \times X\right) \tag{7}$$

$$\mathcal{N}^{(n)}(X) = \text{Norm}\left(\left|\overline{B} \star \mathcal{N}^{(n-1)}(X)\right| \times \mathcal{N}^{(n-1)}(X)\right) \tag{8}$$

The different maps are depicted in Fig. 4. The M^{ver} map detects a sharp vertical gradient on the epidermis, Fig. 4(b). Let us explain the rationale behind equation (1). Because the maps are normalized in the range $[0, 1]$, the product $\times$ of (1) can be understood as a fuzzy 'logical and' operator ([21]): there must be a vertical gradient $|\overline{V} \star I|$ and the image must be strong $|\overline{V} \star I| \times I$. Since the epidermis is supposed to appear once in each column, the $\mathcal{N}$ normalization saturates the value of the most likely point to 1.

The M^{mem} map is designed to be near zero on the membrane, which is itself a region with small horizontal gradients, in which $|I - \overline{H} \star I|$ of equation (2) is small; see the red arrow in Fig. 4(c).

The M^{com} map is a fuzzy 'logical and' between the M^{mem} and the M^{ver} maps, followed by smoothing and normalization, Fig. 4(d). Again, the normalization is justified because the epidermis should be found once in each column.

Finally, the neighbor detection map $\mathcal{N}^{(n)}$ ensures that the epidermis is horizontally continuous, removing bubble artifacts and remaining membrane echos, Fig. 4(e). The neighbor filter $|\overline{B} \star \mathcal{N}^{(n-1)}(X)|$ of equation (7) is a fuzzy 'logical and' operator: the map must be strong and have non-zero neighbors to the left or to the right. The neighbor

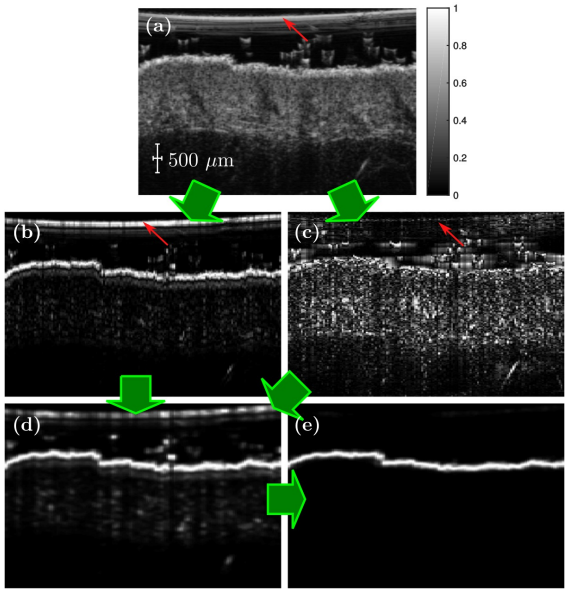

Figure 4. **(a)** Normalized ultrasound image $I(x, z)$ (gray). **(b)** M^{ver} map **(c)** M^{mem} map **(d)** M^{com} map. **(e)** M^{epi} map. Red arrows point at the membrane artifact, which is very strong in the map M^{ver}, absent in map M^{mem} and weak in the combined map M^{com}. Notice that the neighbor map efficiently cleans the map M^{com} to get the final indicator map M^{epi}.

detection filter is applied recursively for $n = 5$ iterations in equation (7), which we found to be sufficient to obtain convergence on the images in the dataset.

The design of this cascade of non-linear maps is largely inspired from deep convolutional neural network ([22]). The proper normalization to the range $M \in [0, 1]$ is crucial so that the recursive application of filters, like the $\mathcal{N}^{(n)}$ mapping, does not produce results diverging to large values or decaying to zero.

The size of the filters are parameters that are set according to the known typical thickness of the epidermis hyperechoic layer (200 μm) and of the typical epidermis irregularities (50 μm). Our tests show that the algorithm is robust to moderate changes in these parameters.

All these map parameters are kept fixed in the rest of the article.

The map $M^{\text{epi}}(x, y, z)$ is then applied onto the image as a mask to exclude the gel/membrane/bubbles area. Specifically, the cumulated map $M^{\text{gel}}(x, y, z) = \sum_{z'<z} M^{\text{epi}}(x, y, z)$ is computed, and in the region $\{(x, y, z)|M^{\text{epi}}(x, y, z) < 1/2\}$ the intensity $I(x, y, z)$ is set to zero.

2.3. Joint segmentation of the epidermis and the dermis

An algorithm of the class of level-set active contour is used for the segmentation or the dermis and the epidermis, using the epidermis indicator map $M^{\text{epi}}(x, y, z)$. The regions of the epidermis E and the epidermis + dermis region ED are implicitly parametrized via two functions, $\phi^{\text{E}}(\mathbf{x})$ and $\phi^{\text{ED}}(\mathbf{x})$, such that $E = \{\mathbf{x}|\phi^{\text{E}}(\mathbf{x}) \geq 0\}$ and $ED = \{\mathbf{x}|\phi^{\text{ED}}(\mathbf{x}) \geq 0\}$. The active contour segmentation is based on the minimization of a loss function $E[\phi^{\text{ED}}, \phi^{\text{E}}]$ designed to suit the problem at hand. The proposed active contour combines 6 terms: two losses E^{I} discriminating the intensity and texture for both E and ED, two regularization terms E^{reg}, a loss E^{map} based on the epidermis indicator map M^{epi} and a self-consistent neighborhood loss E^{neigh} to ensure that the epidermis is continuous:

$$\begin{aligned} E[\phi^{\text{ED}}, \phi^{\text{E}}] &= \alpha E^{\text{reg}}[\phi^{\text{ED}}] + \alpha' E^{\text{reg}}[\phi^{\text{E}}] \\ &+ \beta\, E^{\text{I}}[\phi^{\text{ED}}] + \beta'\, E^{\text{I}}[\phi^{\text{E}}] + \gamma E^{\text{map}}[\phi^{\text{E}}] + \delta E^{\text{neigh}}[\phi^{\text{E}}] \end{aligned} \tag{9}$$

The different terms are weighted by constants $\alpha, \alpha', \beta, \beta', \gamma, \delta$. The different losses are defined as:

- E^{reg} is a standard regularization term ([23]), also known as total variation in the case of convex segmentation ([24]). $E^{\text{reg}}[\phi]$ is equal to the length of the boundary $C = \{\mathbf{x}|\phi(\mathbf{x}) = 0\}$ in 2D or the surface of the boundary $\mathcal{S} = \{\mathbf{x}|\phi(\mathbf{x}) = 0\}$ in 3D. The regularization term is defined for continuous variables as:

$$E^{\text{reg}}[\phi] = \int \mathrm{d}\mathbf{x}\ \delta(\phi(\mathbf{x}))\,|\nabla\phi(\mathbf{x})| \tag{10}$$

  where δ is the Dirac delta distribution.

- The second term $E^{\text{I}}[\phi]$ is a Bayesian log-likelihood term. It is defined to maximize the *a posteriori* likelihood that a given point is inside the region $\phi(\mathbf{x}) \geq 0$ given the distribution of I inside and the outside of the contour ([25, 26]).

  In our model, the distributions are estimated in a non-parametric way, generalizing studies in which assumptions are made on signal statistics ([27, 28]). The $E^{\text{I}}[\phi]$ term reads:

$$E^{\text{I}}[\phi] = -\sum_{\mathbf{x}} \log P(I_{\mathbf{x}}|A[\phi])\mathcal{H}(\phi_{\mathbf{x}}) - \sum_{\mathbf{x}} \log P(I_{\mathbf{x}}|B[\phi])\mathcal{H}(-\phi_{\mathbf{x}}) \tag{11}$$

$$A[\phi] = \{\mathbf{x}|\phi_{\mathbf{x}} \geq 0\} \quad B[\phi] = \{\mathbf{x}|\phi_{\mathbf{x}} < 0\} \tag{12}$$

  where $\mathcal{H}(x)$ is the Heaviside function. $P(I_{\mathbf{x}}|A)$ and $P(I_{\mathbf{x}}|B)$ are the estimated intensity distributions in region A and B, respectively. The distribution $P(I_{\mathbf{x}}|A) = \sum_I \delta(I - I_{\mathbf{x}})P(I|A)$ or $P(I_{\mathbf{x}}|B)$ is obtained with a non-parametric Parzen estimate ([25, 29]) and updated during the optimization process. When the optimum state is reached, every point of the region of interest A is maximally consistent in distribution with all the other points of A.

  Since the non-parametric loss term $E^{\text{I}}[\phi]$ is based on the full distribution $P(I|A)$, it takes into account all local moments of the intensity $\langle I^n \rangle = \sum_I I^n P(I|A)$ and can be understood as an advanced characterization of the local texture.

- The map term is defined as:

$$E^{\text{map}}[\phi^{\text{E}}] = -\sum_{\mathbf{x}} \mathcal{H}(\phi^{\text{E}}_{\mathbf{x}}) \log\left(\frac{M^{\text{epi}}_{\mathbf{x}}}{M_0}\right) \tag{13}$$

  It tends to put inside the epidermis region areas with $M^{\text{epi}}_{\mathbf{x}} > M_0$ and exclude areas with $M^{\text{epi}}_{\mathbf{x}} < M_0$.

- The neighbor term is defined as:

$$E^{\text{neigh}}[\phi^{\text{E}}] = -\sum_{\mathbf{x}} \mathcal{H}(\phi^{\text{E}}_{\mathbf{x}})\ \mathcal{N}^{(1)}(\mathcal{H}(\phi^{\text{E}}_{\mathbf{x}})) \tag{14}$$

defined with the neighbor map (7). The factor $\mathcal{N}^{(1)}(\mathcal{H}(\phi^{\text{E}}_{\mathbf{x}}))$ is high for points which are in the lateral vicinity of the region $\phi^{\text{E}}_{\mathbf{x}} > 0$. $E^{\text{neigh}}[\phi^{\text{E}}]$ favors lateral continuity for the epidermis.

The minimization of $E[\phi^{\text{ED}}, \phi^{\text{E}}]$ in (9) gives the dermis region:

$$D = \{\mathbf{x} \mid \overline{\phi^{\text{ED}}}_{\mathbf{x}} \geq 0 \ \text{ and } \ \overline{\phi^{\text{E}}}_{\mathbf{x}} < 0\} \tag{15}$$

$$\overline{\phi^{\text{ED}}}, \overline{\phi^{\text{E}}} = \text{argmin}_{\phi^{\text{ED}}, \phi^{\text{E}}}\ E[\phi^{\text{ED}}, \phi^{\text{E}}] \tag{16}$$

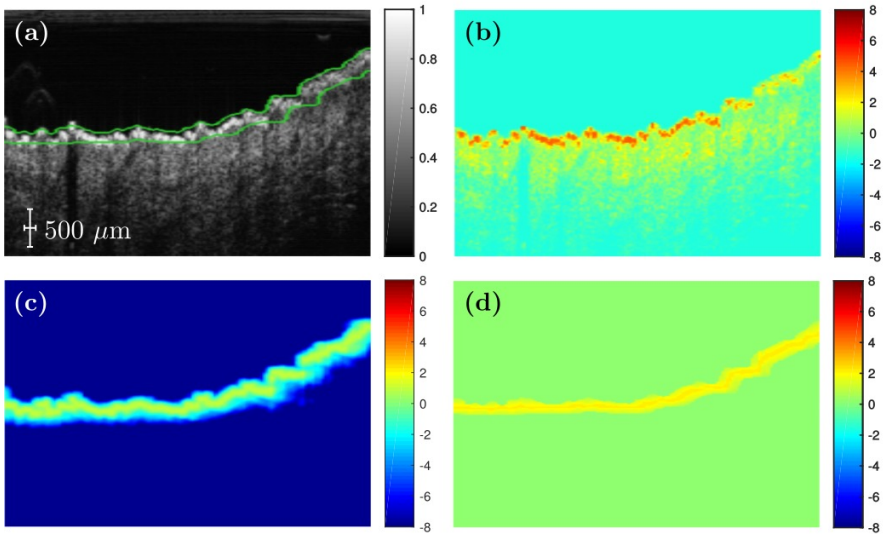

Figure 5. **(a)** Normalized ultrasound image $I(x, z)$ (gray) and edges of the level-set function (green) for the epidermis $\phi^{\mathrm{E}}(\mathbf{x}, t) = 0$ during convergence in the optimization process. **(b)** $f^{\mathrm{I}}(x, z)$ map for the log-likelihood term. Strong positive areas (red) are included in priority as part of the epidermis. Notice that on the right of the image the epidermis is less contrasted. **(c)** $f^{\mathrm{map}}(x, z)$ map in equation (21). The map is strongly positive on the epidermis and negative elsewhere. **(d)** Neighbor map $f^{\mathrm{neigh}}(x, z)$ (22), enforcing the continuity of the segmentation.

The equations of the gradient descent of equation (11) with respect to $\phi^{\mathrm{E}}_{\mathbf{x}}$ and $\phi^{\mathrm{ED}}_{\mathbf{x}}$ are:

$$\frac{\partial \phi^{\mathrm{ED}}(\mathbf{x})}{\partial t} = \delta(\phi^{\mathrm{ED}}(\mathbf{x}))\left[\alpha f^{\mathrm{reg}}_{[\phi^{\mathrm{ED}}]}(\mathbf{x}) + \beta f^{\mathrm{I}}_{[\phi^{\mathrm{ED}}]}(\mathbf{x})\right] \tag{17}$$

$$\frac{\partial \phi^{\mathrm{E}}(\mathbf{x})}{\partial t} = \delta(\phi^{\mathrm{E}}(\mathbf{x}))\left[\alpha' f^{\mathrm{reg}}_{[\phi^{\mathrm{E}}]}(\mathbf{x}) + \beta' f^{\mathrm{I}}_{[\phi^{\mathrm{E}}]}(\mathbf{x}) + \gamma f^{\mathrm{map}}(\mathbf{x}) + \delta f^{\mathrm{neigh}}_{[\phi^{\mathrm{E}}]}(\mathbf{x})\right] \tag{18}$$

$$f^{\mathrm{reg}}[\phi](\mathbf{x}) = \mathrm{div}\left(\frac{\nabla \phi_{\mathbf{x}}}{|\nabla \phi_{\mathbf{x}}|}\right) \tag{19}$$

$$f^{\mathrm{I}}(\mathbf{x}) = \log\left(\frac{\hat{P}(I_{\mathbf{x}}|A[\phi])}{\hat{P}(I_{\mathbf{x}}|B[\phi])}\right) \tag{20}$$

$$f^{\mathrm{map}}(\mathbf{x}) = \log\left(\frac{M^{\mathrm{epi}}_{\mathbf{x}}}{M_0}\right) \tag{21}$$

$$f^{\mathrm{neigh}}(\mathbf{x}) = \mathcal{N}^{(1)}(\mathcal{H}(\phi^{\mathrm{E}}_{\mathbf{x}})) \tag{22}$$

The gradient descent performed is standard and can be found for example in ([26]). In order to illustrate the role of the different terms, Fig. 5 shows $I(x, z)$, $f^{\mathrm{I}}(x, z)$, $f^{\mathrm{map}}(x, z)$ and $f^{\mathrm{neigh}}(x, z)$ half-way during the gradient descent. The indicator map $f^{\mathrm{map}}(x, z)$ in Fig. 5(c) provides a very robust descriptor of location of the epidermis. The intensity and texture term $f^{\mathrm{I}}(x, z)$ of Fig. 5(a) is better resolved spatially, and increases the accuracy. The map $f^{\mathrm{neigh}}(x, z)$ plays a less prominent role but improves the segmentation by preventing the occurrence of jumps in the epidermis segmentation.

2.4. Characterization of the SLEB

The SLEB is a subepidermal low-echoic thin layer of skin, situated in the upper part of the dermis, below the epidermis ([11, 12, 13, 14]). To characterize it, we use the previously described accurate segmentation of the dermis and we scan the entire dermis in thin slices, and finaly analyze the layer-by-layer local statistics of the ultrasound envelope signal. Figure 6(a) shows the bottom line of the dermis h_0, the top line of the dermis h_1, and interpolated lines $h_{0.2}$, $h_{0.4}$, $\cdots$, which are used to scan through the dermis.

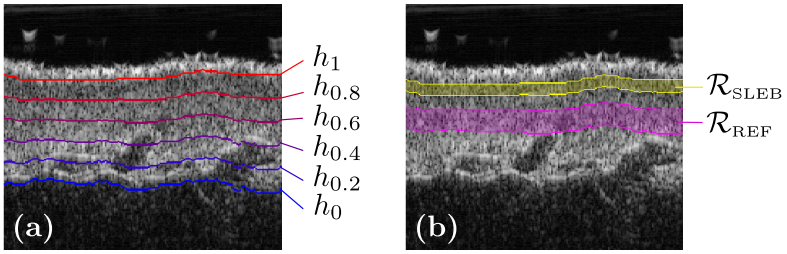

Figure 6. **(a)** Lines used to define the dermis layers. h_0 is the bottom of the dermis, h_1 the top of the dermis. Both are obtained from the automatic segmentation. Arbitrary slices $h_{0.2}, h_{0.4}, \cdots$ are then made via interpolation. **(b)** The regions $\mathcal{R}_{\text{SLEB}}$ and $\mathcal{R}_{\text{REF}}$ used to compute the contrast C. The regions are defined in the text.

It was shown previously in Figure 2 that the Nakagami distribution is a good statistical model of the envelope signal E_v for thin layers. It is indeed known to be a generally reliable yet simple way to characterize an ultrasound signal ([20, 17]). The Nakagami distribution is defined as:

$$P^{\text{Nakagami}}(E_v; m, \Omega) = \frac{2m^m}{\Gamma(m)\Omega^m} E_v^{2m-1} \mathrm{e}^{-m\frac{E_v^2}{\Omega}} \tag{23}$$

The distribution has two free parameters Ω and m; Ω is proportional to the locally reflected power; $m > 0$ is a shape factor, and for $m = 1$ the distribution is a Rayleigh distribution. In the following Ω and m are estimated in thin layers using a least square fit. The average of the envelope signal is then computed as

$$\mu = \frac{\Gamma(m + 1/2)}{\Gamma(m)} \left(\frac{\Omega}{m}\right)^{1/2} \tag{24}$$

Notice that this estimate of the mean envelope is more resistant to outliers than a direct computation of the mean on the envelope.

With these definitions, the SLEB is characterized in the following way:

- The dermis is scanned layer-by-layer from the top 95% to the 65% height in thin slices of a height of 10% of the dermis. The mean envelope μ is computed according to (24). The layer with smallest μ is identified as the SLEB region $\mathcal{R}_{\text{SLEB}}$ and its μ value is called μ_{SLEB}. Figure 6(b) shows an example of an image of the skin with the identified $\mathcal{R}_{\text{SLEB}}$.

- A region $\mathcal{R}_{\text{REF}}$ in the center of the dermis is chosen as a echogenicity reference in the dermis. This reference layer $\mathcal{R}_{\text{REF}}$ is chosen to be the slice at 50%-70% of the dermis height. Its μ value is computed and called μ_{REF}.

- We then define the score of **contrast** C of the SLEB with respect to a reference region situated in the middle of the dermis as:

$$C = \frac{\mu_{\text{REF}} - \mu_{\text{SLEB}}}{\mu_{\text{REF}} + \mu_{\text{SLEB}}} \tag{25}$$

  The contrast C is 1 at most and decreases when the SLEB is less marked. Values of C around zero denote a skin without SLEB, and values close to 1 denote a marked SLEB.

2.5. Characterization of the dermis roughness

We propose another score for skin aging based on skin roughness. Skin roughness has been used for example to characterize scars or striae distensae with a dedicated instrument, the PRIMOS ([30, 31]). We compute roughness from the height map h_1 of the top of the dermis. We perform a high-pass filtering of h_1, $H(h_1) = h_1 - M(h_1)$, where

$M(h_1)$ is a moving average filter with a 2.5 mm window. We choose a roughness measurement based on the standard deviation of $H(h_1)$:

$$R = \text{std}(H(h_1)) \tag{26}$$

With this definition, roughness is a measurement of the typical height fluctuations on horizontal scales smaller than 2.5 mm. The roughness is measured in μm. As the roughness is defined as the standard deviation of all height fluctuations over the lateral span, a low density of large height fluctuations will give a low roughness, possibly lower than the vertical resolution (30 μm).

2.6. Implementation

The method is implemented in Matlab (MathWorks, Inc., Natick, Massachusetts, United States), with a few compiled C++ subroutines. The computation time on an i7-4770 CPU is of 10 minutes for a 3D image of size $300 \times 300 \times 769$ pixels, or $16 \times 16 \times 3.12$ mm and 15 s on a 2D image. In the processing chain, the level-set segmentation accounts for more than 95% of computation time, the filtering steps being comparatively fast. This is not surprising, because the level-set segmentation is the stage where a global self-consistent assessment of the boundaries is made, whereas the filtering steps are purely local computations.

2.7. Acquisition and data set

We conducted a prospective study based on a cohort of 76 healthy women. The ultrasound 2D images were acquired on the external face of the left forearm, a naturally photo-aged skin area. The imaging system was a Dermcup (Atys Medical, Soucieu-En-Jarrest, France), with a 50 MHz mechanical probe, an axial resolution of 30 μm and a lateral resolution of 120 μm. All acquisitions were done with the same parameters: a gain of 10 dB and a depth of 0.16 *mm* under the membrane.

The well documented SCINEXA score is used ([32]) as a visual score of skin aging. We evaluated skin aging on ultrasound images in two groups: group 1 was made up of 38 women aged between 20 and 30 years and had a SCINEXA score < 2. Group 2 consisted of 38 subjects older than 60 with a SCINEXA score ≥ 2.

To limit the data variability, all volunteers were of phototype II or III based on the Fitzpatrick scale ([16]) and non-smokers. No volunteer with a dermatological affliction like eczema or psoriasis was included during the study. Manual segmentations of the epidermis+dermis layer were made on 20 images (11 in group 1, 9 in group 2) by two experts and a blind manual classication in groups 1 and 2 was made on 76 images by 4 experts. Two 3D images were additionally acquired, on one subject from each group. The study is conducted according to the european law for cosmetics trials and approved by the responsible ethics commitee "Comité de Protection des Personnes Sud-Ouest et Outre-mer III". Written consent was obtained for each person participating in the study, and all images have been anonymized.

3. Results

3.1. Validation of the segmentation method

In order to validate the proposed algorithm, the task of the segmentation of the dermis+epidermis layer is attacked with two previously proposed methods:

- The Chan-Vese method ([23]) is a standard all-purpose segmentation algorithm. The Chan-Vese method is an active contour with the same regularization E^{reg} as equation (9), and a loss function which is quadratic in the intensity. In the tests, the level-set function is initialized to positive values in $A = \{\mathbf{x} | I_{\mathbf{x}} > \text{median}_{\mathbf{x}}(I_{\mathbf{x}})\}$.

- The method of ([33]) is an algorithm dedicated to the segmentation of the skin in ultrasound images. It is an active contour based on the Sobel edge operator. This method has been shown to improve the results of a previous method ([34]), another algorithm proposed for the segmentation of the dermis. The level-set function is initialized to positive values in a horizontal slice chosen manually by an expert, enclosing the dermis. This method can not be initialized automatically, since it yields diverging results for inappropriate initial conditions.

The algorithms cited above are the state-of-the-art algorithms for the segmentation of the dermis in high-frequency ultrasound images.

The accuracy of the automatic segmentation is validated using the 20 annotated images. The accuracy is measured using the symmetric Mean Absolute Distance (MAD) and the Dice index D. The MAD of a segmented area A with respect to a manual segmentation GT is defined as the mean of the shortest distance $d(\mathbf{x} \rightarrow GT)$ between a point $\mathbf{x}$ at the boundary of the segmented contour ∂A (here ∂ means the boundary) to the reference GT, and vice versa:

$$\mathrm{MAD} = \frac{1}{N(\partial A)} \sum_{\mathbf{x} \in \partial A} d(\mathbf{x} \rightarrow GT) + \frac{1}{N(\partial GT)} \sum_{\mathbf{x} \in \partial GT} d(\mathbf{x} \rightarrow A) \tag{27}$$

with $N(\partial A)$ the number of pixels in the boundary ∂A. The Dice index is defined as:

$$D = \frac{2N(A \cap GT)}{N(A) + N(GT)} \tag{28}$$

where $\cap$ denotes the set intersection. The Dice index $D \in [0, 1]$ tends to 1 for a perfect segmentation and decreases with false positives and false negatives.

For each method, the parameters of the segmentation have been chosen to give optimal results on the 20 annotated cases in terms of the Dice coefficient:

- For the Chan-Vese method ([23]), the smoothing term is set to $\alpha = 0.8$.
- For the Gao method ([33]), the smoothing term is set to $\alpha = 7$.
- For the proposed method, the constants from equation (9) are set to $\alpha = 0.6$, $\alpha' = 0.3$, $\gamma = 1$, $\delta = 2$ ($\beta = 1$, $\beta' = 1$). The value of the regularization parameters α and α' are chosen according to the expected regularity of the contours ([26]), inferred from the contours drawn by the experts. The chosen value of $\gamma = 1$ and $\delta = 2$ indicate that a roughly balanced importance is given to all terms in equation (9). Our tests have shown that the segmentation is robust to moderate variations (of 30%) of these parameters.

Table 1 shows the accuracy of the segmentation measured with MAD and D for the inter-observer variation and for all two experts and three methods on the 20 annotated cases. The proposed method has best accuracy. The average MAD is 61% lower than that of the Chan-Vese method, and 37% lower than that of the Gao method. Moreover, the Dice index is at the level of inter-observer variation for the proposed method and has lower values for the Chan-Vese and Gao methods.

Figure 7 shows the result of the different segmentation methods on 6 representative cases. The proposed method yields accurate results on the 6 cases shown. The Chan-Vese method is unstable to membrane artifacts, and excludes a marked SLEB with low echogenicity, making it unsuitable, as shown with white arrows in Fig. 7. The Gao method is sensitive to the initialization and generally yields erratic results. This is because the loss function has spurious minima, because the Sobel filter map is not specific enough to characterize the epidermis only, but is also strong for bubbles and for membrane echo artifacts. In many cases, the contour does not converge to the dermis boundary at all, as shown with white arrows in Fig. 7. This can be understood since the method was designed for images with fewer artifacts and resolution, in particular the method of ([34]) was designed for images at 25 MHz with a lower resolution, and more homogeneous images.

3.2. Segmentation and characterization in 3D images

We demonstrate the use of the characterization proposed on two 3D images of the skin, depicted in Fig. 8. The 3D segmentation and characterization uses the same parameters as the 2D segmentation. The two cases considered here are one young skin in Fig. 8(a) and one aged skin in Fig. 8(b). The roughness and contrast scores are of $R = 2.4\ \mu m$, $C = 0$ for the young case and $R = 7.3\ \mu m$, $C = 0.23$ for the aged case. The same computation has been done on all individual 2D slices. The average, median and standard deviation values of the contrast are respectively 0.234, 0.239 and 0.064. The computed mean contrast is consistent with the 3D computation. We observe inhomogeneity in the SLEB contrast of around 20 %.

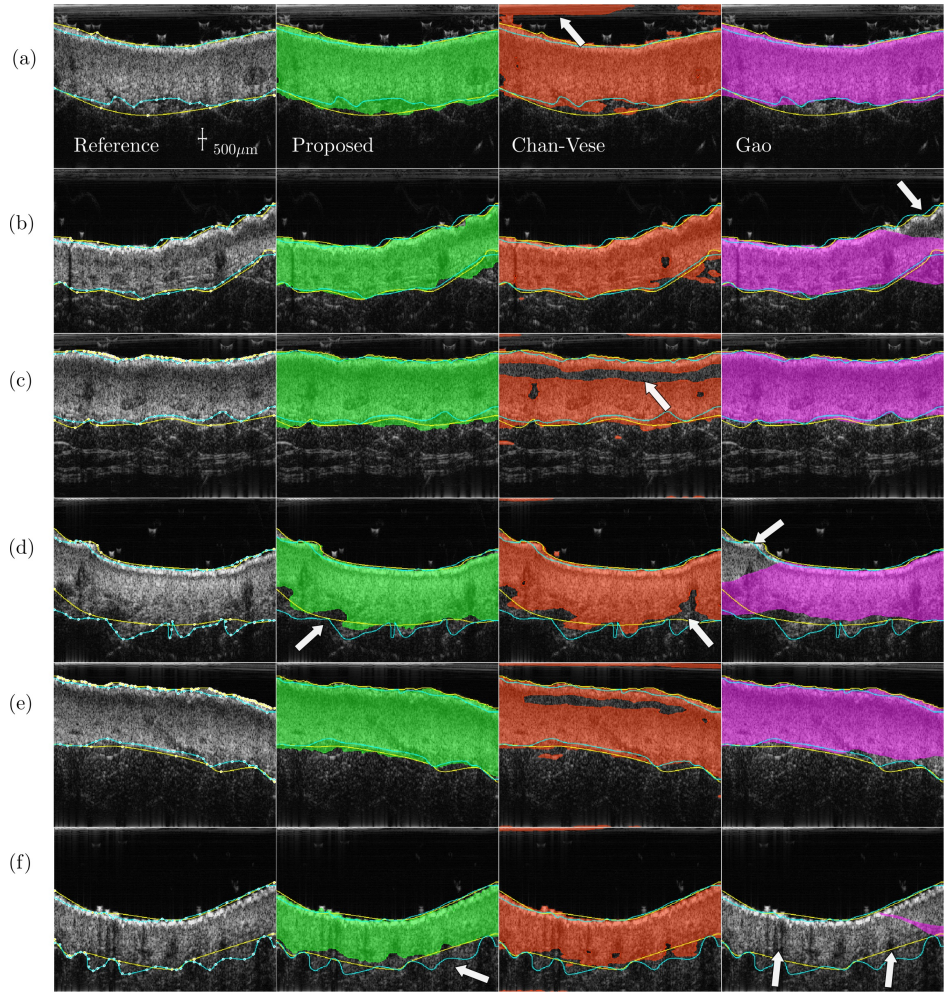

Figure 7. Results of the segmentation on 6 cases (a-f) for the dermis+epidermis area. First column: example of manual segmentations by two experts (yellow and cyan line). The expert contours are repeated in each column. Second column: segmentation with the proposed method (green area). Third column: Chan-Vese method ([23]) (orange area). Fourth column: method of Gao *et al.* ([33]) (purple area). The arrows point at different qualitative errors. In case (f), for the method of Gao the upper and lower lines of the contours have nearly collapsed on the same line.

Table 1. MAD and Dice for the proposed method, the Chan-Vese method ([23]) and the Gao method ([33]) and the inter-observer variability. The mean, median and standard deviation over the dataset is shown for each score.

MAD (μm)	mean	median	std
proposed	**62**	**45**	47
Chan-Vese	160	150	65
Gao	99	65	118
Inter-obs	55	55	21

D	mean	median	std
proposed	**0.93**	**0.94**	0.055
Chan-Vese	0.90	0.90	0.046
Gao	0.82	0.93	0.28
Inter-obs	0.94	0.94	0.024

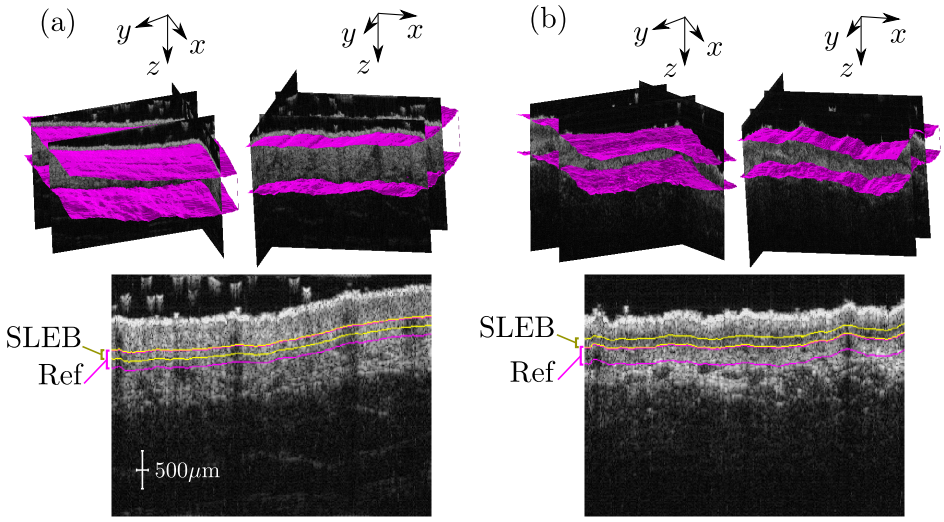

Figure 8. Segmentation and characterization in a 3D image of a **(a)** Young skin with contrast $C = 0$. There is clinically no SLEB. **(b)** Aged skin with contrast $C = 0.23$. Top: 3D rendering of the segmentation of the dermis. Bottom: Boundaries of the reference layer 'Ref' in purple and SLEB layer with lowest intensity in yellow. Both layers are used for the contrast in equation (25).

3.3. Characterization of the skin

The 76 ultrasound images from the experimental study were segmented and analyzed to characterize the SLEB and dermis roughness in groups 1 and 2. To compare with the most broadly used score to characterize the SLEB, we compute one of the most employed score of the SLEB, the mean gray value ratio (MGVR) ([12, 13, 14]). Using manually drawn contours of the dermis, the upper layer $\mathcal{L}_{\text{up}}$ is defined as the area within 50% to 90% of the dermis height. The lower layer $\mathcal{L}_{\text{low}}$ is defined as the area within 10% to 50% of the dermis height. In both areas, the mean of the log-compressed signal ("gray-value") is computed, which we call the I_{up} and I_{low}. The MGVR is defined as $\text{MGVR} = I_{\text{up}}/I_{\text{low}}$. This score lacks robustness, as it depends on the log-compression and filters used in the images. Moreover, in previous works the method relies on manually drawn dermis contours. In this work, the MGVR is also computed on manual contours to demonstrate the advantage of using automatic segmentation tools.

Figure 9 shows the distribution of the three aging scores - MGVR, contrast C and roughness R for the two groups G1 and G2. Figure 9 shows that the contrast C and the roughness R have a better discriminating power than the MGVR, the two groups being better separated. This observation is substantiated with a statistical test. We conduct a two-sample t-test on the MGVR scores of group 1 and group 2 to test whether the difference in mean is statistically significant. The statistical test is an attempt to reject the null hypothesis that the MGVR in group 1 and group 2 derive from a common normal distribution with the same mean. The null hypothesis is rejected at the 5% confidence level, with a significance level $p = 0.046$. The same test is made with the contrast C and roughness R. The null hypothesis is rejected with orders of magnitude lower p-values, $p = 8.3 \times 10^{-8}$ and $p = 8.6 \times 10^{-7}$ respectively, which shows that the two proposed scores have orders of magnitude better performance than the MGVR.

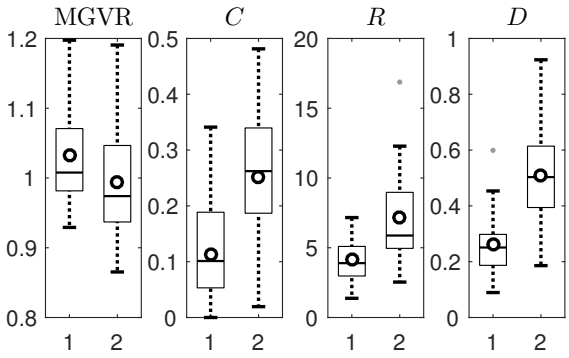

Figure 9. Box plots for the scores MGVR, Contrast C, Roughness R and mixed score D in the two groups, G1 and G2. The contrast and roughness are better scores, since there is less overlap between the two groups. Moreover, a paired t-test shows that the rejection of a null hypothesis of equal means is rejected with much higher confidence with C and R than with MGVR: p-values are 0.046, 8.3×10^{-8}, 8.6×10^{-7} and 1.2×10^{-10} for MGVR, contrast C and roughness R and D respectively.

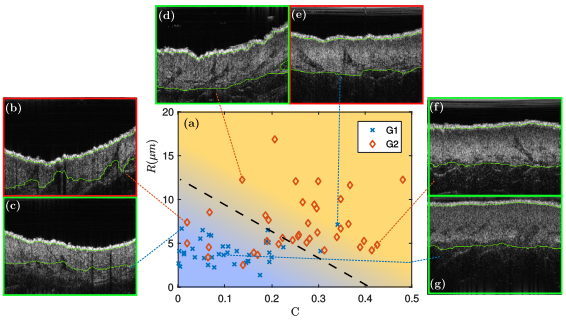

Figure 10. **(a)** Plot of the roughness R (μm) versus contrast C. The two groups are clearly separated using the two cores of SLEB contrast C and roughness R. Background color: most discriminating linear combination $D = C + 0.036 \times R$. Lines of constant color are lines with constant D defined in the text. Black dashed line: optimal separation using a threshold on D with only 12 misclassified cases. **(b-g)** Images of various cases with the automatically segmented dermis (green lines). The images with green border **(c, d, f, g)** are correctly classified and with red border **(b, e)** are two cases of incorrect classification.

The two scores C and R can be combined as $D = C + \eta R$ with $\eta = 0.036\ \mu m^{-1}$. This mixed score is also shown in Fig. 9. This linear combination is represented by shades of colors in Fig. 10(a), where the data for the pairs C, R are shown for the two groups. The two-sample t-test on D rejects the null hypothesis with $p = 1.2 \times 10^{-10}$, which indicates that the combined score D has even greater discriminating power. The parameter $\eta = 0.036$ was chosen to optimize the p-value.

Figure 10 shows a scatter plot of R and C for the two groups. The mixed score D can is also shown in shades of color. The two groups are well separated using the proposed scores R, C and D.

In order to illustrate the performance of the different scores, we attempt to do an *a posteriori* classification of the different cases into the two groups. Specifically, we attempt to attribute each case to group 1 or group 2, using a simple threshold on the MGVR, which yields a MGVR-based classifier. Similarly, we classify the data with a C-based, R-based and D-based classifier. The optimal thresholding is computed based on the known labels. Results are shown in Table 2. The MGVR performs poorly, with a top classification of 50%, not better than a random classifier. On the other hand, C and R have a 80% and 76% accuracy, and the combined scores D has 84% accuracy. For comparison, we

	MGVR	C	R	D	Experts
Correct (in %)	50%	80%	76%	**84%**	80%

Table 2. Correct classification into group 1 and 2, for a threshold classification using the scores MGVR, C, R and the combined score D. The last column is the mean result of a blind manual classification by 4 experts.

ask 4 experts to make a blind classification between group 1 and 2 based on the images. The human experts achieve only 80% accuracy.

Finally, we observe that the 16% misclassified cases are confusing cases with an atypical SLEB or an abnormally inhomogeneous skin. Figure 10(c, d, f, g) illustrate typical cases with a correct classification. Figure 10(b) shows a case with high inhomogeneity but no SLEB, mistaken for young skin. Figure 10(e) shows a case with a marked SLEB, although the subject belongs to group 1.

4. Discussion

In this paper, a framework was proposed for automatic joint segmentation and characterization for the assessment of skin aging. One of the main topics of this work is to propose a local statistical analysis of the dermis layer by layer. This is made possible by the development of an automatic segmentation method. We saw in Figures 4 to 6 how the artifacts can be eliminated and the parallel layers can be detected entirely automatically, and how a quantitative score for skin aging can be derived from their statistical characterization. The Dice index in Table 1 shows that the proposed method is at the level of inter-observer variation and therefore can help clinicians to perform quantitative scoring or skin aging. Figure 9 shows that the signal statistics fitted to the Nakagami distribution and the contrast parameter C vary strongly with depth. These results support the hypothesis that the use of automatic segmentation to find the region of interest is crucial to extract significant scores. Table 2 shows that the combined score D is as precise as human visual inspection and this shows that the proposed method could also be useful in assisting practitionners in clinical study recruitment tasks. Although we have validated the proposed segmentation method on a restricted set of 20 cases, it did lead to meaningful results on all 76 patients. The proposed method has more parameters to control than the previous ones. However we found that the parameters α, α' were easy to adjust because they only affect the regularity of the contours. Overall, this method yielded very good results in a broad range of parameter values. Moreover, it provides an algorithm for segmenting the epidermal layer, which allows to assert the roughness parameter R. The results of table 2 show that the roughness parameter is a very relevant indicator, more than the MGVR, but also that it can be combined with the contrast C to yield an even better aging indicator D.

Aged skin exhibited a more contrasted SLEB and a rougher surface compared to the younger skin. The simultaneous appearing of the SLEB and wrinkles is in accordance with the previous clinical knowledge on skin ageing. However, we noticed that a few patients from the aged group exhibited neither a clear SLEB, nor a rough skin surface. This may be attributed to different habits, such as solar exposure and protection, or genetics. When trying to perform blind classification, these cases are misclassified both by the experts and by the automatic algorithm (cf. Figure 10).

A major factor in the development of skin cancer is excessive UV exposure ([35]). Yet it is difficult to evaluate the history of sun exposure for a given person. Questionnaires have been built to quantify sun related behaviors ([36]) but they often present poor reliability. The intensity of photo-aging on healthy aged skin is probably a good indicator of the risk of skin cancer appearing: SLEB analysis is a simple and convenient method that could be easily incorporated into the physician's routine.

5. Conclusion

In this study, we have proposed a method for the evaluation of skin aging by analyzing 50 MHz ultrasound images, at higher resolution than in the previous studies. We have shown the necessity and advantage of using a joint characterization and segmentation method to perform accurate statistical analysis of the signal in regions that are of physiological interest. Analysing the dermis layer-by-layer, on the whole image, yields far more accurate results than the traditional "sliding window" technique. Our segmentation method did work entirely automatically, with no user intervention, on the whole dataset of images. This was possible thanks to two advanced techniques: the first is hand-crafted non-linear filtering, inspired from deep neural networks and the second is an advanced variational segmentation technique. After identifying the exact location of the dermis, we also proposed a more rigorous analysis than the commonly used mean gray level value. Here, the signal image statistics are fitted to a Nakagami distribution, which is found to be a good approximation of the actual image distribution. Unlike the mean gray level value, this analysis is not dependent on the specific processing of the envelope images by each device, and it is also more physically grounded. Moreover, this approach is more robust towards outliers. We also proposed a measurement

of skin roughness in ultrasound images, which allows the calculation of SLEB contrast and roughness in one single acquisition. Previously, skin roughness could only be evaluated with optical methods. We have carefully validated the accuracy of the segmentation and of the whole processing chain by comparing to existing algorithms. The relevance of the SLEB contrast and skin roughness scores is demonstrated here on a clinical cohort of 76 volunteers. The scores are found to outperform previous skin characterization methods. Unlike previous studies, our method is fully automatic, which is important for obtaining more reproducible results. Automatic algorithms are also instrumental for conducting larger clinical studies, for which the cost of manual segmentation by experts is often a limiting factor. This algorithm may open the door to larger scale studies in skin aging, as well as foster further research on the prevention of photo-aging and associated diseases.

Acknowledgements

This work was funded by the ANR-14-LAB3-0006-01 LabCom AtysCrea and was supported by the LABEX CeLyA (ANR-10-LABX-0060) of the Université de Lyon, within the "Investissements d'Avenir" program (ANR-11-IDEX-0007) operated by the French National Research Agency (ANR).

References

[1] J. M. Waller, H. I. Maibach, Age and skin structure and function, a quantitative approach (i): blood flow, ph, thickness, and ultrasound echogenicity, Skin Research and Technology 11 (4) (2005) 221–235.
[2] D. J. Tobin, Introduction to skin aging, Journal of tissue viability.
[3] M. Farage, K. Miller, P. Elsner, H. Maibach, Intrinsic and extrinsic factors in skin ageing: a review, International Journal of Cosmetic Science 30 (2) (2008) 87–95.
[4] D. Parkin, D. Mesher, P. Sasieni, 13. cancers attributable to solar (ultraviolet) radiation exposure in the uk in 2010, British journal of cancer 105 (2011) S66–S69.
[5] J. K. Robinson, Sun exposure, sun protection, and vitamin d, Jama 294 (12) (2005) 1541–1543.
[6] A. Esteva, B. Kuprel, R. A. Novoa, J. Ko, S. M. Swetter, H. M. Blau, S. Thrun, Dermatologist-level classification of skin cancer with deep neural networks, Nature 542 (7639) (2017) 115–118.
[7] J. M. Waller, H. I. Maibach, Age and skin structure and function, a quantitative approach (ii): protein, glycosaminoglycan, water, and lipid content and structure, Skin Research and Technology 12 (3) (2006) 145–154.
[8] K. S. Nehal, D. Gareau, M. Rajadhyaksha, Skin imaging with reflectance confocal microscopy, in: Seminars in cutaneous medicine and surgery, Vol. 27, Frontline Medical Communications, 2008, pp. 37–43.
[9] E. Wurm, C. Longo, C. Curchin, H. Soyer, T. Prow, G. Pellacani, In vivo assessment of chronological ageing and photoageing in forearm skin using reflectance confocal microscopy, British Journal of Dermatology 167 (2) (2012) 270–279.
[10] C. Longo, A. Casari, F. Beretti, A. M. Cesinaro, G. Pellacani, Skin aging: in vivo microscopic assessment of epidermal and dermal changes by means of confocal microscopy, Journal of the American Academy of Dermatology 68 (3) (2013) e73–e82.
[11] J. Sandby-møller, H. C. Wulf, Ultrasonographic subepidermal low-echogenic band, dependence of age and body site, Skin Research and Technology 10 (1) (2004) 57–63.
[12] M. Gniadecka, Effects of ageing on dermal echogenicity, Skin Research and Technology 7 (3) (2001) 204–207.
[13] F. Lacarrubba, A. Tedeschi, B. Nardone, G. Micali, Mesotherapy for skin rejuvenation: assessment of the subepidermal low-echogenic band by ultrasound evaluation with cross-sectional b-mode scanning, Dermatologic therapy 21 (s3) (2008) S1–S5.
[14] B. Querleux, T. Baldeweck, S. Diridollou, J. De Rigal, E. Huguet, F. Leroy, V. Holloway Barbosa, Skin from various ethnic origins and aging: an in vivo cross-sectional multimodality imaging study, Skin Research and Technology 15 (3) (2009) 306–313.
[15] A. K. Langton, M. J. Sherratt, C. E. M. Griffiths, R. E. B. Watson, Review article: A new wrinkle on old skin: the role of elastic fibres in skin ageing, International Journal of Cosmetic Science 32 (5) (2010) 330–339. doi:10.1111/j.1468-2494.2010.00574.x.
[16] T. Fitzpatrick, The validity and practicality of sun-reactive skin types i through vi, Archives of Dermatology 124 (6) (1988) 869–71.
[17] A. Larrue, J. A. Noble, Modeling of errors in nakagami imaging: Illustration on breast mass characterization, Ultrasound in Medicine & Biology 40 (5) (2014) 917 – 930.
[18] M. Han, J. Wan, Y. Zhao, X. Zhou, M. Wan, Nakagami–m parametric imaging for atherosclerotic plaque characterization using the coarse-to-fine method, Ultrasound in Medicine & Biology 43 (6) (2017) 1275 – 1289.
[19] M. Byra, A. Nowicki, H. Wróblewska-Piotrzkowska, K. Dobruch-Sobczak, Classification of breast lesions using segmented quantitative ultrasound maps of homodyned k distribution parameters, Medical Physics 43 (10) (2016) 5561–5569.
[20] F. Destrempes, G. Cloutier, A critical review and uniformized representation of statistical distributions modeling the ultrasound echo envelope, Ultrasound in Medicine and Biology 36 (7) (2010) 1037 – 1051.
[21] I. Bloch, Fuzzy spatial relationships for image processing and interpretation: a review, Image and Vision Computing 23 (2) (2005) 89–110.
[22] I. Goodfellow, Y. Bengio, A. Courville, Deep Learning, MIT Press, 2016.
[23] T. Chan, L. Vese, Active contours without edges, Image Processing, IEEE Transactions on 10 (2) (2001) 266–277.
[24] X. Bresson, S. Esedoḡlu, P. Vandergheynst, J.-P. Thiran, S. Osher, Fast global minimization of the active contour/snake model, Journal of Mathematical Imaging and Vision 28 (2) (2007) 151–167. doi:10.1007/s10851-007-0002-0.

[25] J. Kim, J. Fisher, A. Yezzi, M. Cetin, A. Willsky, A nonparametric statistical method for image segmentation using information theory and curve evolution, Image Processing, IEEE Transactions on 14 (10) (2005) 1486–1502.
[26] B. Sciolla, L. Cowell, T. Dambry, B. Guibert, P. Delachartre, Segmentation of skin tumors in high-frequency 3-d ultrasound images, Ultrasound in medicine & biology 43 (1) (2017) 227–238.
[27] A. Sarti, C. Corsi, E. Mazzini, C. Lamberti, Maximum likelihood segmentation of ultrasound images with Rayleigh distribution, Ultrasonics, Ferroelectrics, and Frequency Control, IEEE Transactions on 52 (6) (2005) 947–960.
[28] M. Pereyra, N. Dobigeon, H. Batatia, J. Tourneret, Segmentation of skin lesions in 2D and 3D ultrasound images using a spatially coherent generalized rayleigh mixture model, Medical Imaging, IEEE Transactions on 31 (8) (2012) 1509–1520.
[29] O. Michailovich, Y. Rathi, A. Tannenbaum, Image segmentation using active contours driven by the bhattacharyya gradient flow, IEEE Transactions on Image Processing 16 (11) (2007) 2787–2801.
[30] M. C. Bloemen, M. S. van Gerven, M. B. van der Wal, P. D. Verhaegen, E. Middelkoop, An objective device for measuring surface roughness of skin and scars, Journal of the American Academy of Dermatology 64 (4) (2011) 706–715.
[31] M. Bleve, P. Capra, F. Pavanetto, P. Perugini, Ultrasound and 3d skin imaging: methods to evaluate efficacy of striae distensae treatment, Dermatology research and practice 2012.
[32] A. Vierkötter, U. Ranft, U. Krämer, D. Sugiri, V. Reimann, J. Krutmann, The scinexa: a novel, validated score to simultaneously assess and differentiate between intrinsic and extrinsic skin ageing, Journal of dermatological science 53 (3) (2009) 207–211.
[33] Y. Gao, A. Tannenbaum, H. Chen, M. Torres, E. Yoshida, X. Yang, Y. Wang, W. Curran, T. Liu, Automated skin segmentation in ultrasonic evaluation of skin toxicity in breast cancer radiotherapy, Ultrasound in Medicine & Biology 39 (11) (2013) 2166 – 2175.
[34] J.-M. Lagarde, J. George, R. Soulcié, D. Black, Automatic measurement of dermal thickness from b-scan ultrasound images using active contours, Skin Research and Technology 11 (2) (2005) 79–90.
[35] R. Kwa, K. Campana, R. Moy, Biology of cutaneous squamous cell carcinoma, Journal of the American Academy of Dermatology 26 (1) (1992) 1–26.
[36] B. Køster, J. Søndergaard, J. Nielsen, A. Olsen, J. Bentzen, Reliability and consistency of a validated sun exposure questionnaire in a population-based danish sample, Preventive Medicine Reports 10 (2018) 43–48.